Artificial compressibility Godunov fluxes for variable density incompressible flows

F. Bassi[a], F. Massa[a,*], L. Botti[a], A. Colombo[a]

[a] *Università degli Studi di Bergamo, Dipartimento di Ingegneria e Scienze Applicate*

Abstract

In this work we present and compare three Riemann solvers for the artificial compressibility perturbation of the 1D variable density incompressible Euler equations. The goal is to devise an artificial compressibility flux formulation to be used in Finite Volume or discontinuous Galerkin discretizations of the variable density incompressible Navier-Stokes equations. Starting from the constant density case, two Riemann solvers taking into account density jumps at fluid interfaces are first proposed. By enforcing the divergence free constraint in the continuity equation, these approximate Riemann solvers deal with density as a purely advected quantity. Secondly, by retaining the conservative form of the continuity equation, the exact Riemann solver is derived. The variable density solution is fully coupled with velocity and pressure unknowns. The Riemann solvers are compared and analysed in terms of robustness on harsh 1D Riemann problems. The extension to multidimensional problems is described. The effectiveness of the exact Riemann solver is demonstrated in the context of high-order accurate discontinuous Galerkin discretization of variable density incompressible flow problems. We numerically validate the implementation considering the Kovasznay test case and the Rayleigh-Taylor instability problem.

Keywords: Variable density incompressible flows, artificial compressibility, Riemann solver, discontinuous Galerkin method

*Corresponding author: francescocarlo.massa@unibg.it, Tel +39 0352052150, fax +39 0352052077

1. Introduction

The numerical solution of both the constant and the variable density Incompressible Navier-Stokes (INS) equations is a challenging task. On the one hand explicit integration in time is usually not employed due to the algebraic nature of the incompressibility constraint, on the other hand fully coupled velocity-pressure formulations result in systems of DAEs that are expensive to solve due to the saddle point nature of the problem. Decoupled time integration strategies based on projection methods, see Chorin [7] and Temam [13], and artificial compressibility methods, see Chorin [6], have been widely employed to improve the effectiveness of the solution strategy. A pressure correction scheme for variable density incompressible flows was devised by Guermond and Quartapelle [9] while Pyo and Shen proposed a Gauge-Uzawa method [12].

In the context of discontinuous Galerkin (dG) formulations of incompressible flow problems, the artificial compressibility concept has been employed to recover hyperbolicity at inter-element boundaries and devise a suitable Godunov numerical flux for velocity-pressure coupling, see *e.g.* [3, 4]. Since artificial compressibility is introduced only at the interface flux level to obtain a physically meaningful coupling between pressure and velocity, the resulting INS equations discretization is consistent irrespectively of the amount of artificial compressibility introduced. The artificial compressibility flux allows for equal degree velocity-pressure formulations and provides robustness when dealing with convection-dominated flow regimes but it only mitigates the difficulties involved in the solution process. In the context of fully coupled dG formulations of the INS equations efficiency might be pursued with ad hoc preconditioners, for example a recent work by Botti et al. [5] reports promising results by means of agglomeration based h-multigrid solution strategies.

In this work we seek to extend the dG method introduced in [3] by Bassi et al. to variable density incompressible flows. In particular, we introduce the exact and two approximate Riemann solvers for the artificial compressibility perturbation of the 1D variable density incompressible Euler equations. In the approximate Riemann solvers we add a transport equation for the density unknown to the constant density artificial compressibility equations devised by Elsworth and Toro [8] in their Riemann solver. Then we consider two choices for the density in the momentum

equation, *i.e.*, either a constant reference density or the variable physical density. In the former case velocity and pressure solutions are decoupled from density fluctuations while in the latter velocity and pressure are influenced by density jumps across the contact discontinuity. In the exact Riemann solver the conservative continuity equation is considered in place of the density transport equation. Only in this setting the density solution might differ from the left and right states. Interestingly, the exact Riemann solver admits an explicit solution, therefore it is also the most efficient. The solvers are designed to be applied in the direction normal to element faces and are well suited to be employed in the context of high order dG discretizations. To this end we provide a multidimensional extension for each of the proposed solvers.

The paper is organized as follows: in Section 3 and Section 4 we present the approximate Riemann solvers while in Section 5 we derive the exact Riemann solver. In Section 7.1 we consider five benchmark Riemann problems to compare the numerical fluxes provided by exact and approximate Riemann solvers. Next we turn to the dG discretization of the variable density INS equations, where artificial compressibility is introduced only at the flux level. The convergence properties of the dG formulation is assessed on the 2D Kovasnzay test case in Section 7.2. Finally, the robustness of the formulation is assessed considering the Rayleigh-Taylor instability problem in Section 7.3.

2. Governing equations of the 1D Riemann problem

The 1D variable density incompressible Euler equations, modified by means of an artificial compressibility term, are

$$\begin{aligned} \frac{1}{\rho_0 c^2}\frac{\partial p}{\partial t} + \frac{\partial u}{\partial x} &= 0, \\ \frac{\partial(\rho u)}{\partial t} + \frac{\partial(\rho u^2 + p)}{\partial x} &= 0, \\ \frac{\partial \rho}{\partial t} + \frac{\partial(\rho u)}{\partial x} &= 0, \end{aligned} \tag{1}$$

where p is the pressure, u the velocity and ρ is the density. Here $c \in \mathbb{R}\setminus\{0\}$ is the artificial compressibility coefficient and $\rho_0 = 1$ is a reference density.

Starting from the initial piecewise constant data p_L, u_L, ρ_L, and p_R, u_R, ρ_R, that distinguish

Table 1: Sets of equations for the three Riemann solvers here considered.

CDRS	SDRS	ERS
$\frac{1}{\rho_0 c^2}\frac{\partial p}{\partial t} + \frac{\partial u}{\partial x} = 0$	$\frac{1}{\rho_0 c^2}\frac{\partial p}{\partial t} + \frac{\partial u}{\partial x} = 0$	$\frac{1}{\rho_0 c^2}\frac{\partial p}{\partial t} + \frac{\partial u}{\partial x} = 0$
$\frac{\partial(\rho_0 u)}{\partial t} + \frac{\partial(\rho_0 u^2 + p)}{\partial x} = 0$	$\frac{\partial(\rho u)}{\partial t} + \frac{\partial(\rho u^2 + p)}{\partial x} = 0$	$\frac{\partial(\rho u)}{\partial t} + \frac{\partial(\rho u^2 + p)}{\partial x} = 0$
$\frac{\partial \rho}{\partial t} + u\frac{\partial \rho}{\partial x} = 0$	$\frac{\partial \rho}{\partial t} + u\frac{\partial \rho}{\partial x} = 0$	$\frac{\partial \rho}{\partial t} + \frac{\partial(\rho u)}{\partial x} = 0$

left (L) and right (R) initial states respectively, we wish to find the solution of the 1D Riemann problem for model (1). The solution consists of four states separated by two centred waves, hereafter called "left" and "right" waves, and a contact discontinuity (see Fig. 1). Left and right waves can be either rarefactions or shocks depending on the initial values and across them all the unknowns can change. Instead, in the region between waves, called *star region* ($\star$), pressure and normal velocity are constant and only the density can vary.

In Tab. 1 we report, for the sake of comparison, the sets of equations for the Riemann solvers considered in this work. The first two solvers (CDRS and SDRS) are exact solvers based on modified sets of equations as compared to problem (1) and thus they give rise to approximate solutions. In particular

- CDRS (Constant Density Riemann Solver) is the Riemann solver proposed by Elsworth and Toro [8] for constant density flows. Here, to account for density variations, we simply augment the original set of equations with the density transport equation. Note that a reference density ρ_0 equal to one is employed in the momentum equation.

- SDRS (Switched Density Riemann Solver) is the exact Riemann solver for problem (1) except that the continuity equation is simplified imposing a solenoidal velocity field. As a result the density is a purely advected property.

- ERS is the Exact Riemann Solver for model (1).

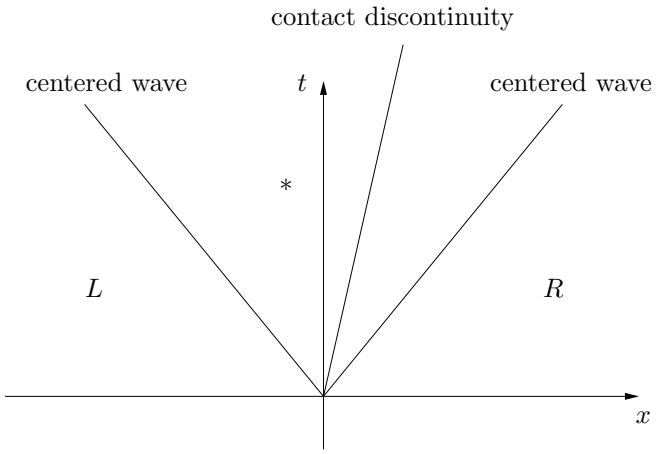

Figure 1: Structure of the Riemann problem.

3. Constant density approximate Riemann solver (CDRS)

The exact 1D Riemann solver devised by Elsworth and Toro in [8] for constant density incompressible flows is based on the following hyperbolic set of equations

$$\begin{aligned} \frac{1}{\rho_0 c^2}\frac{\partial p}{\partial t} + \frac{\partial u}{\partial x} &= 0, \\ \frac{\partial(\rho_0 u)}{\partial t} + \frac{\partial(\rho_0 u^2 + p)}{\partial x} &= 0. \end{aligned} \tag{2}$$

Setting

$$\frac{D\rho}{Dt} = \frac{\partial \rho}{\partial t} + u\frac{\partial \rho}{\partial x} = 0, \tag{3}$$

we consider the density as a purely advected property, *i.e.*, a property that can change only across the contact discontinuity. Moreover, according to Eq. (2), pressure and velocity solutions inside the star region are decoupled from the density fluctuations and can be obtained by means of the solver of [8]. The density solution reads

$$\rho_{\star L} = \rho_L, \qquad \text{and} \qquad \rho_{\star R} = \rho_R. \tag{4}$$

4. Switched density approximate Riemann solver (SDRS)

As for the constant density Riemann solver, the switched density Riemann solver enforces the divergence free constraint inside the continuity equation of problem (1). Accordingly, the density is a purely advected property, and its solution inside the star region reads

$$\rho_{\star L} = \rho_L, \qquad \text{and} \qquad \rho_{\star R} = \rho_R. \tag{5}$$

Since the density can vary only across the contact discontinuity, the first two equations of problem (1) can be rewritten as

$$\begin{aligned} \frac{1}{\rho_0 c^2}\frac{\partial p}{\partial t} + \frac{\partial u}{\partial x} &= 0, \\ \frac{\partial u}{\partial t} + \frac{\partial (u^2 + p/\hat{\rho})}{\partial x} &= 0, \end{aligned} \tag{6}$$

where the constant density $\hat{\rho}$ takes the left (resp. the right) value on the left (resp. on the right) of the contact discontinuity. In compact form, system (6) reads

$$\frac{\partial \mathbf{w}}{\partial t} + \frac{\partial \mathbf{F}(\mathbf{w})}{\partial x} = \mathbf{0}, \tag{7}$$

with

$$\mathbf{w} = \begin{bmatrix} p \\ u \end{bmatrix}, \qquad \mathbf{F}(\mathbf{w}) = \begin{bmatrix} \rho_0 c^2 u \\ u^2 + \dfrac{p}{\hat{\rho}} \end{bmatrix}. \tag{8}$$

The flux Jacobian matrix is given by

$$\mathbf{A} = \frac{\partial \mathbf{F}(\mathbf{w})}{\partial \mathbf{w}} = \begin{bmatrix} 0 & \rho_0 c^2 \\ \dfrac{1}{\hat{\rho}} & 2u \end{bmatrix}, \tag{9}$$

and eigenvalues vector $\boldsymbol{\lambda}$ and left and right eigenvector matrices $\mathbf{L}$ and $\mathbf{R}$ are

$$\boldsymbol{\lambda} = \begin{bmatrix} u-a \\ \\ u+a \end{bmatrix},$$

$$\mathbf{L} = \begin{bmatrix} \dfrac{1}{\hat{\rho}} & u-a \\ \\ \dfrac{1}{\hat{\rho}} & u+a \end{bmatrix}, \tag{10}$$

$$\mathbf{R} = \frac{1}{2a} \begin{bmatrix} \hat{\rho}\,(u+a) & -\hat{\rho}\,(u-a) \\ \\ -1 & 1 \end{bmatrix},$$

where

$$a = \sqrt{u^2 + \hat{c}^2}, \qquad \hat{c}^2 = \frac{\rho_0}{\hat{\rho}} c^2. \tag{11}$$

According to the definition of c and a it is clear that $\lambda_- = (u-a) < 0$ and $\lambda_+ = (u+a) > 0$. Left and right waves can be rarefactions or shocks and the solution across them is computed by means of Riemann invariants and Rankine-Hugoniot jump conditions, respectively.

4.1. Rarefaction waves and Riemann invariants

The solution across a rarefaction wave can be obtained by means of Riemann invariants $\boldsymbol{\Gamma}$. Indeed, invariants are conserved inside this kind of wave and in particular they assume constant values along the characteristic curves

$$C_\pm(x,t) = x + \lambda_\pm t. \tag{12}$$

By definition, the gradients of the Riemann invariants are the left eigenvectors $\mathbf{L}_i$ of matrix $\mathbf{A}$, where $i = 1, 2$ is the row number of matrix $\mathbf{L}$. It follows that

$$\begin{aligned} d\Gamma_- &= \mathbf{L}_1 \cdot d\mathbf{w} = \frac{1}{\hat{\rho}} dp + (u-a)\, du = 0 \qquad \text{on} \qquad C_-, \\ d\Gamma_+ &= \mathbf{L}_2 \cdot d\mathbf{w} = \frac{1}{\hat{\rho}} dp + (u+a)\, du = 0 \qquad \text{on} \qquad C_+. \end{aligned} \tag{13}$$

Therefore, the Riemann invariants are

$$\begin{aligned}\Gamma_- &= \frac{p}{\hat{\rho}} + \frac{1}{2}\left[u\,(u-a) - \hat{c}^2 \ln\,(u+a)\right] = const. \quad \text{on} \quad C_-,\\ \Gamma_+ &= \frac{p}{\hat{\rho}} + \frac{1}{2}\left[u\,(u+a) + \hat{c}^2 \ln\,(u+a)\right] = const. \quad \text{on} \quad C_+,\end{aligned} \tag{14}$$

and we recall that the left rarefaction is crossed by C_+ characteristic lines and the right rarefaction by C_- characteristic lines.

4.2. Shock waves and Rankine-Hugoniot jump conditions

The jumps of variables $\Delta\mathbf{w} = \mathbf{w}_2 - \mathbf{w}_1$ and of fluxes $\Delta\mathbf{F} = \mathbf{F}\,(\mathbf{w}_2) - \mathbf{F}\,(\mathbf{w}_1)$ across a shock are related to each other by means of the Rankine-Hugoniot conditions

$$\Delta\mathbf{F} = s\Delta\mathbf{w}, \tag{15}$$

where s is the shock speed. Applied to (8),(15) gives

$$\begin{aligned}\rho_0 c^2 \Delta u &= s\Delta p,\\ \Delta u^2 + \frac{\Delta p}{\hat{\rho}} &= s\Delta u.\end{aligned} \tag{16}$$

It follows that

$$\begin{aligned}\frac{p_2 - p_1}{\hat{\rho}} &= \hat{c}^2 \frac{u_2 - u_1}{s},\\ s_\pm &= \frac{u_2 + u_1}{2} \pm \sqrt{\left(\frac{u_2 + u_1}{2}\right)^2 + \hat{c}^2},\end{aligned} \tag{17}$$

where $s_- < 0$ and $s_+ > 0$ are the left and right shock speeds, respectively.

4.3. Star region pressure and velocity solutions

The Riemann solution in the star region is obtained as a function of the initial piecewise constant data exploiting the Riemann invariants and the Rankine-Hugoniot conditions across rarefaction (superscript R) and shock (superscript S) waves, respectively. Recalling the solution for the density given by (5), we impose $\hat{\rho} = \rho_L$ for the left wave and $\hat{\rho} = \rho_R$ for the right wave.

- If the left wave is a rarefaction then the Γ_+ Riemann invariant is preserved

$$\Gamma_{+\star} = \Gamma_{+L}, \tag{18}$$

that means

$$p_\star = p_L + f_L^R(u_L, \rho_L, u_\star), \tag{19}$$

with

$$\begin{aligned} f_L^R(u_L, \rho_L, u_\star) \overset{\text{def}}{=} \frac{1}{2}\rho_L \Big[& u_L\,(u_L + a_L) + c_L^2 \ln(u_L + a_L) \\ & - u_\star\,(u_\star + a_{\star L}) - c_L^2 \ln(u_\star + a_{\star L}) \Big], \end{aligned} \tag{20}$$

where

$$a_L = \sqrt{u_L^2 + c_L^2}, \qquad a_{\star L} = \sqrt{u_\star^2 + c_L^2}, \qquad c_L^2 = \frac{\rho_0}{\rho_L} c^2. \tag{21}$$

- If the left wave is a shock then from relations (17) it follows that

$$p_\star = p_L + f_L^S(u_L, \rho_L, u_\star), \tag{22}$$

with

$$f_L^S(u_L, \rho_L, u_\star) \overset{\text{def}}{=} \rho_L c_L^2 \frac{u_\star - u_L}{s_{\star L}}, \tag{23}$$

where

$$s_{\star L} = \frac{u_\star + u_L}{2} - \sqrt{\left(\frac{u_\star + u_L}{2}\right)^2 + c_L^2}, \qquad c_L^2 = \frac{\rho_0}{\rho_L} c^2. \tag{24}$$

- If the right wave is a rarefaction then the Γ_- Riemann invariant is conserved

$$\Gamma_{-R} = \Gamma_{-\star}, \tag{25}$$

that is

$$p_\star = p_R + f_R^R(u_R, \rho_R, u_\star), \tag{26}$$

with

$$f_R^R(u_R,\rho_R,u_\star) \stackrel{\text{def}}{=} \frac{1}{2}\rho_R\Big[u_R\left(u_R-a_R\right)-c_R^2\ln\left(u_R+a_R\right) \\ -u_\star\left(u_\star-a_{\star R}\right)+c_R^2\ln\left(u_\star+a_{\star R}\right)\Big], \tag{27}$$

where

$$a_R=\sqrt{u_R^2+c_R^2}, \qquad a_{\star R}=\sqrt{u_\star^2+c_R^2}, \qquad c_R^2=\frac{\rho_0}{\rho_R}c^2. \tag{28}$$

- If the right wave is a shock then relations (17) can be applied to get

$$p_\star = p_R + f_R^S(u_R,\rho_R,u_\star), \tag{29}$$

with

$$f_R^S(u_R,\rho_R,u_\star) \stackrel{\text{def}}{=} \rho_R c_R^2\frac{u_\star-u_R}{s_{R\star}}, \tag{30}$$

where

$$s_{R\star}=\frac{u_R+u_\star}{2}+\sqrt{\left(\frac{u_R+u_\star}{2}\right)^2+c_R^2}, \qquad c_R^2=\frac{\rho_0}{\rho_R}c^2. \tag{31}$$

Comparing Eqs. (19), (22), (26) and (29), it follows that

$$F(p_L,u_L,\rho_L,p_R,u_R,\rho_R,u_\star)=p_R-p_L+f_R(u_R,\rho_R,u_\star)-f_L(u_L,\rho_L,u_\star)=0, \tag{32}$$

where $f_R(u_R,\rho_R,u_\star)$ and $f_L(u_L,\rho_L,u_\star)$ must be set according to the nature of centred waves

$$f_L(u_L,\rho_L,u_\star)=\begin{cases} f_L^S(u_L,\rho_L,u_\star) & u_\star<u_L \\ f_L^R(u_L,\rho_L,u_\star) & \text{otherwise,}\end{cases} \\ f_R(u_R,\rho_R,u_\star)=\begin{cases} f_R^S(u_R,\rho_R,u_\star) & u_R<u_\star \\ f_R^R(u_R,\rho_R,u_\star) & \text{otherwise,}\end{cases} \tag{33}$$

where the inequalities $u_R<u_\star$ and $u_\star<u_L$ satisfy the entropy condition for right and left shocks respectively, *i.e.*, shocks are always compressive (see first relation of (17) for proof).

The solution of the nonlinear Eq. (32) by means of the Newton's method gives the velocity $u_\star$ in the star region

$$\begin{cases} u_\star^{k+1} = u_\star^k - \dfrac{F(u_\star^k)}{F'(u_\star^k)} \\ u_\star^0 = \dfrac{u_R + u_L}{2}. \end{cases} \tag{34}$$

At each iteration k the function F is the one appropriate for the wave pattern defined by Eq. (33). Typically, convergence to a relative tolerance of 10^{-14} is achieved in 4 or 5 iterations. For the sake of completeness, we report the derivative functions with respect to $u_\star$

$$\begin{aligned} f_L^{'S}(u_L, \rho_L, u_\star) &= \left.\frac{\partial f_L^S}{\partial u_\star}\right|_{u_L, \rho_L} = 2\rho_L c_L^2 \frac{u_\star - s_{\star L}}{s_{\star L}\left(u_\star + u_L - 2s_{\star L}\right)}, \\ f_L^{'R}(\rho_L, u_\star) &= \left.\frac{\partial f_L^R}{\partial u_\star}\right|_{u_L, \rho_L} = -\rho_L\left(u_\star + a_{\star L}\right), \\ f_R^{'S}(u_R, \rho_R, u_\star) &= \left.\frac{\partial f_R^S}{\partial u_\star}\right|_{u_R, \rho_R} = 2\rho_R c_R^2 \frac{u_\star - s_{R\star}}{s_{R\star}\left(u_\star + u_R - 2s_{R\star}\right)}, \\ f_R^{'R}(\rho_R, u_\star) &= \left.\frac{\partial f_R^R}{\partial u_\star}\right|_{u_R, \rho_R} = -\rho_R\left(u_\star - a_{\star R}\right), \end{aligned} \tag{35}$$

recalling that

$$F'(u_L, \rho_L, u_R, \rho_R, u_\star) = \left.\frac{\partial F}{\partial u_\star}\right|_{u_L, \rho_L, u_R, \rho_R} = f_R'(u_R, \rho_R, u_\star) - f_L'(u_L, \rho_L, u_\star). \tag{36}$$

Finally, given the solution $u_\star$ and Eqs. (33), the pressure $p_\star$ in the star region is computed as

$$p_\star = p_R + f_R(u_R, \rho_R, u_\star) = p_L + f_L(u_L, \rho_L, u_\star). \tag{37}$$

5. Exact Riemann solver

The equations system (1) can be written in the compact form as

$$\frac{\partial \mathbf{w}}{\partial t} + \frac{\partial \mathbf{F}(\mathbf{w})}{\partial x} = \mathbf{0}, \tag{38}$$

where

$$\mathbf{w} = \begin{bmatrix} p \\ \rho u \\ \rho \end{bmatrix}, \qquad \mathbf{F}(\mathbf{w}) = \begin{bmatrix} \rho_0 c^2 u \\ \rho u^2 + p \\ \rho u \end{bmatrix}. \tag{39}$$

The flux Jacobian matrix reads

$$\mathbf{A} = \frac{\partial \mathbf{F}(\mathbf{w})}{\partial \mathbf{w}} = \begin{bmatrix} 0 & \frac{\rho_0}{\rho} c^2 & -\frac{\rho_0}{\rho} c^2 u \\ 1 & 2u & -u^2 \\ 0 & 1 & 0 \end{bmatrix}, \tag{40}$$

with eigenvalues vector $\boldsymbol{\lambda}$ and left and right eigenvector matrices $\mathbf{L}$ and $\mathbf{R}$

$$\boldsymbol{\lambda} = \begin{bmatrix} \lambda_- \\ \lambda_0 \\ \lambda_+ \end{bmatrix} = \begin{bmatrix} \frac{u-a}{2} \\ u \\ \frac{u+a}{2} \end{bmatrix},$$

$$\mathbf{L} = \begin{bmatrix} \frac{1}{a\lambda_+} & \frac{\lambda_-}{a\lambda_+} & -\frac{\lambda_-\lambda_0}{a\lambda_+} \\ \frac{1}{\lambda_-\lambda_+} & \frac{\lambda_0}{\lambda_-\lambda_+} & -\frac{\lambda_+^2 + \lambda_-\lambda_0}{\lambda_-\lambda_+} \\ -\frac{1}{a\lambda_-} & -\frac{\lambda_+}{a\lambda_-} & \frac{\lambda_0\lambda_+}{a\lambda_-} \end{bmatrix} = \begin{bmatrix} \frac{2}{a(u+a)} & \frac{u-a}{a(u+a)} & -\frac{u(u-a)}{a(u+a)} \\ -\frac{\rho}{\rho_0 c^2} & -\frac{\rho u}{\rho_0 c^2} & \frac{\rho u^2 + \rho_0 c^2}{\rho_0 c^2} \\ -\frac{2}{a(u-a)} & -\frac{u+a}{a(u-a)} & \frac{u(u+a)}{a(u-a)} \end{bmatrix}, \tag{41}$$

$$\mathbf{R} = \begin{bmatrix} \lambda_+^2 & 0 & \lambda_-^2 \\ \lambda_- & \lambda_0 & \lambda_+ \\ 1 & 1 & 1 \end{bmatrix} = \begin{bmatrix} \frac{(u+a)^2}{4} & 0 & \frac{(u-a)^2}{4} \\ \frac{u-a}{2} & u & \frac{u+a}{2} \\ 1 & 1 & 1 \end{bmatrix},$$

where

$$a = \sqrt{u^2 + 4\frac{\rho_0}{\rho} c^2} \tag{42}$$

According to the definition of c and a it is clear that $\lambda_- < 0$, $\lambda_+ > 0$ and $\lambda_- < \lambda_0 < \lambda_+$.

5.1. Rarefaction waves and Riemann invariants

Riemann invariants are conserved across rarefaction waves and assume constant values along the characteristic curves

$$C(x,t) = x + \lambda t, \tag{43}$$

that means

$$d\Gamma_- = \mathbf{L}_1 \cdot d\mathbf{w} = dp + \frac{u-a}{2} d(\rho u) - u\frac{u-a}{2} d\rho = 0 \qquad \text{on} \qquad C_-, \tag{44}$$

$$d\Gamma_0 = \mathbf{L}_2 \cdot d\mathbf{w} = dp + u d(\rho u) - \left(u^2 + \frac{\rho_0}{\rho} c^2\right) d\rho = 0 \qquad \text{on} \qquad C_0, \tag{45}$$

$$d\Gamma_+ = \mathbf{L}_3 \cdot d\mathbf{w} = dp + \frac{u+a}{2} d(\rho u) - u\frac{u+a}{2} d\rho = 0 \qquad \text{on} \qquad C_+, \tag{46}$$

where $\mathbf{L}_i$ are the left eigenvectors of matrix $\mathbf{A}$, *i.e.*, row vectors of matrix $\mathbf{L}$, or in primitive variables

$$d\Gamma_- = dp + \rho\frac{u-a}{2} du = 0 \qquad \text{on} \qquad C_-, \tag{47}$$

$$d\Gamma_0 = dp + \rho u du - \frac{\rho_0}{\rho} c^2 d\rho = 0 \qquad \text{on} \qquad C_0, \tag{48}$$

$$d\Gamma_+ = dp + \rho\frac{u+a}{2} du = 0 \qquad \text{on} \qquad C_+. \tag{49}$$

Since ρ depends on u, a relation between density and velocity is needed in order to integrate Eqs. (47) and (49) . The sought relation can be found by means of characteristic curves intersection

$$d\Gamma_{0-} = d\Gamma_0 - d\Gamma_- = 2\rho du + (u-a)\, d\rho = 0 \quad \text{on} \quad C_0 \cap C_-, \tag{50}$$

$$d\Gamma_{0+} = d\Gamma_0 - d\Gamma_+ = 2\rho du + (u+a)\, d\rho = 0 \quad \text{on} \quad C_0 \cap C_+. \tag{51}$$

Considering the definition (42) and imposing $u \neq 0$, we can multiply Eqs. (50) and (51) by u and

obtain the relations

$$d\Gamma_{0-} = \frac{\text{sign}(u)}{\sqrt{\rho u^2\left(\rho u^2 + 4\rho_0 c^2\right)}} d(\rho u^2) - \frac{1}{\rho} d\rho = 0 \quad \text{on} \quad C_0 \cap C_-, \tag{52}$$

$$d\Gamma_{0+} = \frac{\text{sign}(u)}{\sqrt{\rho u^2\left(\rho u^2 + 4\rho_0 c^2\right)}} d(\rho u^2) + \frac{1}{\rho} d\rho = 0 \quad \text{on} \quad C_0 \cap C_+, \tag{53}$$

which can be integrated exactly to give

$$const. = \begin{cases} \ln\left[\rho\left(a - u\right)\right] & u < 0 \\ \ln\left(u + a\right) & u > 0 \end{cases} \quad \text{on} \quad C_0 \cap C_-, \tag{54}$$

$$const. = \begin{cases} \ln\left(a - u\right) & u < 0 \\ \ln\left[\rho\left(u + a\right)\right] & u > 0 \end{cases} \quad \text{on} \quad C_0 \cap C_+, \tag{55}$$

or, reminding the eigenvalues definition and noting that $\lambda_- \lambda_+ = -\rho_0 c^2/\rho$,

$$const. = \Gamma_{0-} = \rho\lambda_-, \quad u \neq 0 \quad \text{on} \quad C_0 \cap C_-, \tag{56}$$

$$const. = \Gamma_{0+} = \rho\lambda_+, \quad u \neq 0 \quad \text{on} \quad C_0 \cap C_+. \tag{57}$$

that means for $u \neq 0$

$$\rho = \frac{\Gamma_{0-}^2}{\rho_0 c^2 + u\Gamma_{0-}} \quad \text{on} \quad C_0 \cap C_-, \tag{58}$$

$$\rho = \frac{\Gamma_{0+}^2}{\rho_0 c^2 + u\Gamma_{0+}} \quad \text{on} \quad C_0 \cap C_+. \tag{59}$$

Moreover, imposing $u = 0$ and integrating Eqs. (50) and (51), one obtains

$$\rho = const. \tag{60}$$

along both $C_0 \cap C_-$ and $C_0 \cap C_+$. Then, Eqs. (56), (57) and Eqs. (58), (59), which in the limit $u \to 0$ verify the condition (60), can be considered valid for any value of u.

Using relations (56) and (57) the Riemann invariants associated with the characteristic curves $C_{\pm}$ can be finally defined integrating Eqs. (47) and (49)

$$const. = \Gamma_{-} = p + \Gamma_{0-} u \quad \text{on} \quad C_{-}, \tag{61}$$

$$const. = \Gamma_{+} = p + \Gamma_{0+} u \quad \text{on} \quad C_{+}. \tag{62}$$

5.2. Shock waves and Rankine-Hugoniot jump conditions

Jumps $\Delta \mathbf{w} = \mathbf{w}_2 - \mathbf{w}_1$ and $\Delta \mathbf{F} = \mathbf{F}(\mathbf{w}_2) - \mathbf{F}(\mathbf{w}_1)$ across a shock are related to each other by means of Rankine-Hugoniot conditions

$$\Delta \mathbf{F} = s \Delta \mathbf{w}, \tag{63}$$

where s denotes the shock speed.

Applying (63) to (39) we get the system

$$\begin{aligned} \rho_0 c^2 \Delta u &= s \Delta p, \\ \Delta \left(\rho u^2 \right) + \Delta p &= s \Delta (\rho u), \\ \Delta (\rho u) &= s \Delta \rho, \end{aligned} \tag{64}$$

from which we can derive the pressure and density relations

$$p_2 - p_1 = \rho_0 c^2 \frac{u_2 - u_1}{s}, \tag{65}$$

$$\frac{\rho_2}{\rho_1} = \frac{u_1 - s}{u_2 - s}. \tag{66}$$

Moreover, combining the first two relations of the system (64) with the Eq. (66) it follows the relation

$$\rho_X (u_X - s) + \frac{\rho_0 c^2}{s} = 0, \tag{67}$$

whose solutions are the left (−) and right (+) moving shock speeds

$$s_{\pm} = \frac{u_X \pm a_X}{2}, \qquad a_X = \sqrt{u_X^2 + 4\frac{\rho_0}{\rho_X}c^2}, \tag{68}$$

where due to Eq. (66) X can be either 1 or 2 without any restriction. Notice that $s_- < 0$ and $s_+ > 0$.

5.3. Star region solution

Starting from the initial piece-wise constant datum and basing on Riemann invariants and Rankine-Hugoniot conditions the Exact Riemann problem solution in the star region is now performed. Here again superscript R denotes the rarefaction wave and superscript S the shock wave.

- If the left wave is a rarefaction then Γ_+ and Γ_{0+} Riemann invariants are preserved

$$\begin{aligned} \Gamma_{+\star} &= \Gamma_{+L}, \\ \Gamma_{0+\star} &= \Gamma_{0+L}, \end{aligned} \tag{69}$$

that means

$$\begin{aligned} p_\star &= p_L + f_L^R(u_L, \rho_L, u_\star), \\ \rho_{\star L} &= f_{\rho L}^R(u_L, \rho_L, u_\star), \end{aligned} \tag{70}$$

with

$$\begin{aligned} f_L^R(u_L, \rho_L, u_\star) &\stackrel{\text{def}}{=} \Gamma_{0+L}\,(u_L - u_\star)\,, \\ f_{\rho L}^R(u_L, \rho_L, u_\star) &\stackrel{\text{def}}{=} \frac{\Gamma_{0+L}^2}{\rho_0 c^2 + u_\star \Gamma_{0+L}}, \end{aligned} \tag{71}$$

where

$$\Gamma_{0+L} = \rho_L \frac{u_L + a_L}{2}, \qquad a_L = \sqrt{u_L^2 + 4\frac{\rho_0}{\rho_L}c^2}. \tag{72}$$

- If the left wave is a shock then from relations (65) and (66) it follows that

$$\begin{aligned} p_\star &= p_L + f_L^S(u_L, \rho_L, u_\star), \\ \rho_{\star L} &= f_{\rho_L}^S(u_L, \rho_L, u_\star), \end{aligned} \tag{73}$$

with

$$\begin{aligned} f_L^S(u_L, \rho_L, u_\star) &\stackrel{\text{def}}{=} \rho_0 c^2 \frac{u_\star - u_L}{s_L}, \\ f_{\rho_L}^S(u_L, \rho_L, u_\star) &\stackrel{\text{def}}{=} \rho_L \frac{u_L - s_L}{u_\star - s_L}, \end{aligned} \tag{74}$$

where

$$s_L = \frac{u_L - a_L}{2}, \qquad a_L = \sqrt{u_L^2 + 4\frac{\rho_0}{\rho_L}c^2}. \tag{75}$$

- If the right wave is a rarefaction then Γ_- and Γ_{0-} Riemann invariants are conserved

$$\begin{aligned} \Gamma_{-\star} &= \Gamma_{-R}, \\ \Gamma_{0-\star} &= \Gamma_{0-R}, \end{aligned} \tag{76}$$

that is

$$\begin{aligned} p_\star &= p_R + f_R^R(u_R, \rho_R, u_\star), \\ \rho_{\star R} &= f_{\rho_R}^R(u_R, \rho_R, u_\star), \end{aligned} \tag{77}$$

with

$$\begin{aligned} f_R^R(u_R, \rho_R, u_\star) &\stackrel{\text{def}}{=} \Gamma_{0-R}\left(u_R - u_\star\right), \\ f_{\rho_R}^R(u_R, \rho_R, u_\star) &\stackrel{\text{def}}{=} \frac{\Gamma_{0-R}^2}{\rho_0 c^2 + u_\star \Gamma_{0-R}}, \end{aligned} \tag{78}$$

where

$$\Gamma_{0-R} = \rho_R \frac{u_R - a_R}{2}, \qquad a_R = \sqrt{u_R^2 + 4\frac{\rho_0}{\rho_R}c^2}. \tag{79}$$

- If the right wave is a shock then relations (65) and (66) can be applied to get

$$\begin{aligned} p_\star &= p_R + f_R^S(u_R, \rho_R, u_\star), \\ \rho_{\star R} &= f_{\rho_R}^S(u_R, \rho_R, u_\star), \end{aligned} \tag{80}$$

with

$$\begin{aligned} f_R^S(u_R,\rho_R,u_\star) &\stackrel{\text{def}}{=} \rho_0 c^2 \frac{u_\star - u_R}{s_R}, \\ f_{\rho R}^S(u_R,\rho_R,u_\star) &\stackrel{\text{def}}{=} \rho_R \frac{u_R - s_R}{u_\star - s_R}, \end{aligned} \tag{81}$$

where

$$s_R = \frac{u_R + a_R}{2}, \qquad a_R = \sqrt{u_R^2 + 4\frac{\rho_0}{\rho_R}c^2}. \tag{82}$$

Comparing Eqs. (70), (73), (77) and (80) we derive

$$F(p_L,u_L,\rho_L,p_R,u_R,\rho_R,u_\star) = p_R - p_L + f_R(u_R,\rho_R,u_\star) - f_L(u_L,\rho_L,u_\star) = 0, \tag{83}$$

where $f_R(u_R,\rho_R,u_\star)$ and $f_L(u_L,\rho_L,u_\star)$ must be set accordingly to the nature of centered waves

$$\begin{aligned} f_L(u_L,\rho_L,u_\star) &= \begin{cases} f_L^R(u_L,\rho_L,u_\star) & u_\star < u_L \\ f_L^S(u_L,\rho_L,u_\star) & \text{otherwise,} \end{cases} \\ f_R(u_R,\rho_R,u_\star) &= \begin{cases} f_R^S(u_R,\rho_R,u_\star) & u_R < u_\star \\ f_R^R(u_R,\rho_R,u_\star) & \text{otherwise,} \end{cases} \end{aligned} \tag{84}$$

with the $u_R < u_\star$ and $u_\star < u_L$ inequalities satisfying the entropy condition for the right and left shock respectively, *i.e.* shocks are always compressive. However, we can notice that the pressure-velocity dependence inside the star region is invariant with respect to the wave nature. Indeed, we prove that

$$\begin{aligned} f_L^R(u_L,\rho_L,u_\star) = \Gamma_{0+L}\,(u_L - u_\star) = \rho_L \lambda_{+L}\,(u_L - u_\star) = \\ = \rho_0 c^2 \frac{u_\star - u_L}{\lambda_{-L}} = \rho_0 c^2 \frac{u_\star - u_L}{s_L} = f_L^S(u_L,\rho_L,u_\star), \end{aligned} \tag{85}$$

$$f_R^R(u_R, \rho_R, u_\star) = \Gamma_{0-R}\,(u_R - u_\star) = \rho_R \lambda_{-R}\,(u_R - u_\star) = \\ = \rho_0 c^2 \frac{u_\star - u_R}{\lambda_{+R}} = \rho_0 c^2 \frac{u_\star - u_R}{s_R} = f_R^S(u_R, \rho_R, u_\star). \quad (86)$$

Moreover, from Eq. (71), (74), (78) and (81) it is clear that this dependence is linear thus allowing to compute the star region velocity explicitly

$$u_\star = \frac{p_R - p_L + u_R\Gamma_{0-R} - u_L\Gamma_{0+L}}{\Gamma_{0-R} - \Gamma_{0+L}}. \quad (87)$$

As a consequence, the star region pressure $p_\star$ can be found as

$$p_\star = p_R + f_R^X(u_R, \rho_R, u_\star) = p_L + f_L^X(u_L, \rho_L, u_\star) \quad (88)$$

where we can refer either to the shock ($X = S$) or the rarefaction wave ($X = R$).

Finally, the density is defined by means the function f_ρ

$$\rho_{\star L} = f_{\rho L}^X(u_L, \rho_L, u_\star), \qquad \rho_{\star R} = f_{\rho R}^X(u_R, \rho_R, u_\star), \quad (89)$$

where again f_ρ can be computed independently on the centered waves nature since

$$f_{\rho L}^R(u_L, \rho_L, u_\star) = \frac{\Gamma_{0+L}^2}{\rho_0 c^2 + u_\star \Gamma_{0+L}} = \frac{\rho_L \lambda_{+L}}{-\lambda_{-L} + u_\star} = \rho_L \frac{u_L - s_L}{u_\star - s_L} = f_{\rho L}^S(u_L, \rho_L, u_\star), \quad (90)$$

$$f_{\rho R}^R(u_R, \rho_R, u_\star) = \frac{\Gamma_{0-R}^2}{\rho_0 c^2 + u_\star \Gamma_{0-R}} = \frac{\rho_R \lambda_{-R}}{-\lambda_{+R} + u_\star} \rho_L \frac{u_R - s_R}{u_\star - s_R} = f_{\rho R}^S(u_R, \rho_R, u_\star). \quad (91)$$

5.4. Wave speeds

In order to completely define the exact solution we still need to determine wave speeds S.

- For the rarefaction wave there exist two significant wave speeds associated with the head (h) and the tail (t) of the fan, respectively. More in particular speed values are defined by

the eigenvalues of the states on either side of the rarefaction

$$S^R_{hL} = \lambda_{-L}, \qquad S^R_{tL} = \lambda_{-*L}, \tag{92}$$

$$S^R_{hR} = \lambda_{+R}, \qquad S^R_{tR} = \lambda_{+*R}. \tag{93}$$

- For the shock wave the wave speed is given by the relation (68)

$$S^S_L = s_{-L}, \qquad S^S_R = s_{+R}. \tag{94}$$

- For the contact discontinuity (superscript C) the speed is simply defined by the star region velocity

$$S^C = u_\star. \tag{95}$$

Careful analysis of the above wave speeds leads to interesting remarks. Knowing that the Riemann invariant (56) (resp. (57)) is conserved on the left (resp. right) rarefaction wave it is possible to prove that head and tail speeds coincide, indeed

$$S^R_{hL} = \lambda_{-L} = \frac{-\rho_0 c^2}{\rho_L \lambda_{+L}} = \frac{-\rho_0 c^2}{\rho_{\star L} \lambda_{+*L}} = \lambda_{-*L} = S^R_{tL}, \tag{96}$$

$$S^R_{hR} = \lambda_{+R} = \frac{-\rho_0 c^2}{\rho_R \lambda_{-R}} = \frac{-\rho_0 c^2}{\rho_{\star R} \lambda_{-*R}} = \lambda_{+*R} = S^R_{tR}. \tag{97}$$

This result shows that the exact solution of problem (5) always jumps across centered waves (although the rarefaction wave is expansive and not compressive like the shock one). Moreover, rarefactions and shocks have the same speeds

$$S^S_L = s_{-L} = \lambda_{-L} = S^R_L, \qquad S^S_R = s_{+R} = \lambda_{+R} = S^R_R, \tag{98}$$

thus making the exact solution completely independent from the nature of centered waves. Finally, there exists a critical value of the artificial compressibility coefficient $\overline{c}_X \in \mathbb{C}$ for which the

contact wave is as fast as the left or the right centered wave

$$u_\star = S_X, \tag{99}$$

where $u_\star$ is defined by Eq. (87) and $X = L$ or $X = R$ for the left or the right wave, respectively. Depending on the initial Riemann problem left and right states, the critical artificial compressibility coefficient might be a real number. Interestingly, when $\overline{c}_X \in \mathbb{R}$, for $c^2 < \overline{c}_X^2$, the wave pattern arising from the exact solver predicts a contact wave overtaking the centered wave. Since this configuration violates the wave pattern postulated in Fig. 1, the solver is no longer exact in this occurrence.

A deeper analysis having the goal of determining c values able to preserve the prescribed wave pattern will be addressed in a future work. Note that all Riemann Solvers presented in this work share the issue of potentially violating the wave pattern. In particular also the original Riemann Solver of [8] might admit real values of $\overline{c}_X$ depending on the initial state, even for constant density flows.

6. The Split 3D Riemann problem

As usual with most upwind-type methods, the extension of the 1D Riemann solvers to the 3D case is based on the solution of the x-split Riemann problem

$$\begin{cases} \dfrac{\partial \mathbf{w}}{\partial t} + \dfrac{\partial \mathbf{F}(\mathbf{w})}{\partial x} = \mathbf{0} \\ \mathbf{w}(0) = \mathbf{w}_X, \end{cases} \tag{100}$$

with $\mathbf{w}_X = \mathbf{w}_L$ (resp. $\mathbf{w}_X = \mathbf{w}_R$) for the initial left state (resp. right state) and

$$\mathbf{w} = \begin{bmatrix} p \\ \rho u \\ \rho\theta \\ \rho \end{bmatrix}, \qquad \mathbf{F}(\mathbf{w}) = \begin{bmatrix} \rho_0 c^2 u \\ \rho u^2 + p \\ \rho\theta u \\ \rho u \end{bmatrix}, \tag{101}$$

where x is the local coordinate normal to the inter-element boundary and the variable θ denotes either tangential velocity component v or w. Similarly to the 1D case, $c \in \mathbb{R}\setminus\{0\}$ is the artificial compressibility coefficient and $\rho_0 = 1$ is a reference density.

The wave pattern arising from the split 3D Riemann problem (100) is almost identical to that of the 1D case reported in Fig. 1. Indeed, the pressure and the normal velocity u are constant inside the star region while the tangential velocity component θ and the density can vary across the centred waves and the contact discontinuity.

Tab. 2 collects the sets of x-split governing equations for each of the Riemann solvers considered in this work. Comparing Tab. 2 and Tab. 1, we see that in the x-split 3D case we have the additional x-split momentum equation for the variable θ, *i.e.*, for either tangential velocity component. Hence, the relations that define the properties $p_\star$, $u_\star$, $\rho_{\star L}$ and $\rho_{\star R}$ in the star region are identical to those of the 1D case and only the relations for $\theta_{\star L}$ and $\theta_{\star R}$ must be derived. In particular

- For the CDRS the reference density ρ_0 is employed also in the tangential momentum equations. Therefore the evolution of θ is decoupled from the density variation and can be obtained as shown in [8] and [3].

- For the SDRS it can be noticed that combining the last two equations we get the same conservation equation for the quantity θ used in the CDRS

$$\frac{\partial\theta}{\partial t} + \frac{\partial(\theta u)}{\partial x} = 0. \tag{102}$$

Table 2: Sets of x-split 3D equations for the three Riemann solvers here considered.

CDRS	SDRS	ERS
$\frac{1}{\rho_0 c^2}\frac{\partial p}{\partial t} + \frac{\partial u}{\partial x} = 0$	$\frac{1}{\rho_0 c^2}\frac{\partial p}{\partial t} + \frac{\partial u}{\partial x} = 0$	$\frac{1}{\rho_0 c^2}\frac{\partial p}{\partial t} + \frac{\partial u}{\partial x} = 0$
$\frac{\partial(\rho_0 u)}{\partial t} + \frac{\partial(\rho_0 u^2 + p)}{\partial x} = 0$	$\frac{\partial(\rho u)}{\partial t} + \frac{\partial(\rho u^2 + p)}{\partial x} = 0$	$\frac{\partial(\rho u)}{\partial t} + \frac{\partial(\rho u^2 + p)}{\partial x} = 0$
$\frac{\partial(\rho_0 \theta)}{\partial t} + \frac{\partial(\rho_0 \theta u)}{\partial x} = 0$	$\frac{\partial(\rho \theta)}{\partial t} + \frac{\partial(\rho \theta u)}{\partial x} = 0$	$\frac{\partial(\rho \theta)}{\partial t} + \frac{\partial(\rho \theta u)}{\partial x} = 0$
$\frac{\partial \rho}{\partial t} + u\frac{\partial \rho}{\partial x} = 0$	$\frac{\partial \rho}{\partial t} + u\frac{\partial \rho}{\partial x} = 0$	$\frac{\partial \rho}{\partial t} + \frac{\partial(\rho u)}{\partial x} = 0$

Hence, the expressions for $\theta_{\star L}$ and $\theta_{\star R}$ of the CDRS are valid also for the SDRS.

- For the ERS, combining again the last two equations it follows that the tangential velocity is treated as a purely advected property

$$\frac{D\theta}{Dt} = \frac{\partial \theta}{\partial t} + u\frac{\partial \theta}{\partial x} = 0. \tag{103}$$

This means that θ can only change across the contact discontinuity, whereby

$$\theta_{\star L} = \theta_L, \qquad \text{and} \qquad \theta_{\star R} = \theta_R. \tag{104}$$

7. Results

In this section the proposed Riemann solvers are first assessed on a set of five 1D Riemann problems. The 1D test cases serve the purpose of evaluating and comparing the Riemann solvers both in terms of the numerical fluxes they provide for the considered Riemann problems and in terms of their behaviour when implemented in a dG $\mathbb{P}^0$ solver for the numerical solution of the system (1), *i.e.*, including the artificial compressibility term in the divergence constraint. The reference solutions for these test cases are the exact self-similar solutions of the system (1) provided by the exact Riemann solver.

Then we address 2D test cases which we compute by means of a high-order dG solver for the variable density INS equations. This solver employs the exact Riemann solver to compute

the inviscid numerical fluxes responsible for the velocity-pressure-density coupling. We remark that, as was the case for the constant density INS solver employed in [3, 4], the variable density INS solver does not include any artificial compressibility term in the divergence constraint of the governing equations.

7.1. 1D test cases

Table 3 gathers the initial data of five 1D Riemann problems employed to assess and compare the Riemann solvers for variable density incompressible flows presented in this work, *i.e.*, the constant density Riemann solver (CDRS), the switched density Riemann solver (SDRS) and the exact Riemann solver (ERS).

T1 was proposed by Elsworth and Toro in [8] and was especially conceived to investigate the robustness of Riemann solvers for constant density artificial compressibility equations. T2, T3, T4 were proposed by Toro in [14]. T2 considers a strong pressure jump as initial condition and its solution consists of a strong shock wave, a contact surface and a left rarefaction wave. T3 and T4 challenge the ability of Riemann solvers to reproduce a contact discontinuity in particular an isolated stationary contact wave (T3) and an isolated contact moving slowly to the right (T4). T5 is a modification of T1 conceived to investigate the robustness of Riemann solvers for variable density artificial compressibility equations. We keep the same velocity-pressure left and right states of T1 and introduce a strong density discontinuity as if we were to simulate air on the left and water on the right.

In Table 4 we report the artificial compressibility coefficient with the output time for each Riemann problem. Notice that for test cases T2 and T5 it is possible to a find a real value of $\overline{c}$ on the right or the left wave. In particular, for T2, the critical value is remarkably high thus requiring to use a higher value of the artificial compressibility coefficient in order to ensure the exact solver effectiveness.

In Table 5 we compare the Godunov numerical fluxes provided by the Riemann solvers along the space-time line $x/t = 0$ taking as reference the Godunov fluxes provided by Exact Solver. It is interesting to remark that the fluxes provided by the solvers are identical for test cases T3 and T4 because all the Riemann solvers share the ability of exactly resolving a contact discontinuity,

Table 3: Initial piece-wise constant data for the 5 test Riemann problems.

test	p_L	u_L	ρ_L	p_R	u_R	ρ_R
T1	1.00E−01	1.00E+00	1.00E+00	1.00E+00	1.00E+00	1.00E+00
T2	1.00E+03	0.00E+00	1.00E+00	1.00E−02	0.00E+00	1.00E+00
T3	1.00E+00	0.00E+00	1.40E+00	1.00E+00	0.00E+00	1.00E+00
T4	1.00E+00	1.00E−01	1.40E+00	1.00E+00	1.00E−01	1.00E+00
T5	1.00E−01	1.00E+00	1.25E−03	1.00E+00	1.00E+00	1.00E+00

Table 4: Artificial compressibility coefficients and output time (T) for the 5 test Riemann problems.

test	$\overline{c}_L^2$	$\overline{c}_R^2$	c^2	T
T1	-	-	0.81	0.1
T2	-	499.995	1000	0.005
T3	-	-	1	2
T4	-	-	1	2
T5	0.09398	-	1	0.005

Table 5: Comparison of Riemann solvers for each test Riemann problem.

	solver	$f_1 = \rho_0 c^2 u_\star$		$f_2 = \rho_\star u_\star^2 + p_\star$		$f_3 = \rho_\star u_\star$	
		value	% error	value	% error	value	% error
T1	CDRS	0.51010	11.87	1.2478	2.938	0.62975	20.10
	SDRS	0.51010	11.87	1.2478	2.938	0.62975	20.10
	ERS	0.45597	0.0	1.2122	0.0	0.78813	0.0
T2	CDRS	15302.	3.223	614.92	7.762	153.02	45.16
	SDRS	15302.	3.223	614.92	7.762	153.02	45.16
	ERS	15811.	0.0	666.67	0.0	105.41	0.0
T3	CDRS	0.0	0.0	1.0	0.0	0.0	0.0
	SDRS	0.0	0.0	1.0	0.0	0.0	0.0
	ERS	0.0	0.0	1.0	0.0	0.0	0.0
T4	CDRS	0.1	0.0	1.014	0.0	0.14	0.0
	SDRS	0.1	0.0	1.014	0.0	0.14	0.0
	ERS	0.1	0.0	1.014	0.0	0.14	0.0
T5	CDRS	0.65349	273.7	0.83661	332.7	0.00082	100.7
	SDRS	−0.19027	49.41	0.17889	7.482	−0.19027	63.23
	ERS	−0.37611	0.0	0.19336	0.0	−0.11656	0.0

i.e. $u_L = u_R$ and $p_L = p_R$. Instead, significant differences are observed in test cases T1, T2 and T5. Since in test cases T1 and T2 $\rho_L = \rho_R = \rho_\star = \rho_0$, CDRS and SDRS provide the same fluxes and, hence, the same errors with respect to the exact solution. Test case T5 is the most severe one. Since $\rho_L \ll \rho_0$ and ρ_0 is the actual density employed in the momentum equation, CDRS introduces very large errors, to the point that the contact discontinuity travels in the wrong

Figure 2: Fluxes computed with the three RS proposed at the space-time line $x/t = 0$ for the T5 with artificial compressibility values in the range $c = [1, 1000]$. Percentage errors with respect to the fluxes exact solution (f_x) computed with ERS are reported on the right.

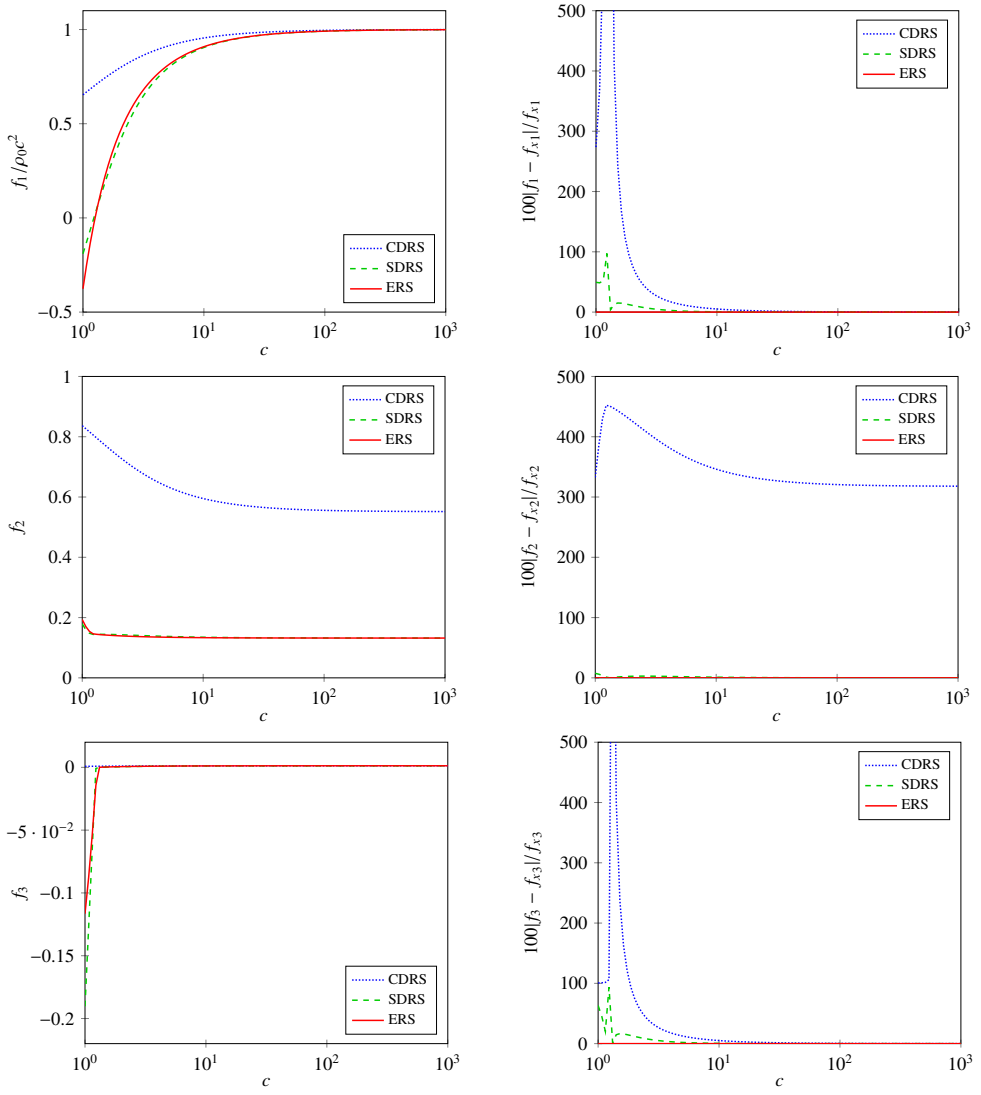

direction (note the opposite sign of the numerical fluxes f_1 and f_3 compared to the exact values in Table 5). SDRS is more accurate than CDRS on T5 providing errors comparable with those observed in T1 and T2.

In Figure 2 we consider most severe Riemann problem T5 and we report the Godunov numerical flux behaviors and relative errors with respect to the exact fluxes provided by ERS while

Figure 3: DG $\mathbb{P}^0$ method with different Riemann solvers applied to test T1. Comparison between numerical and exact solutions.

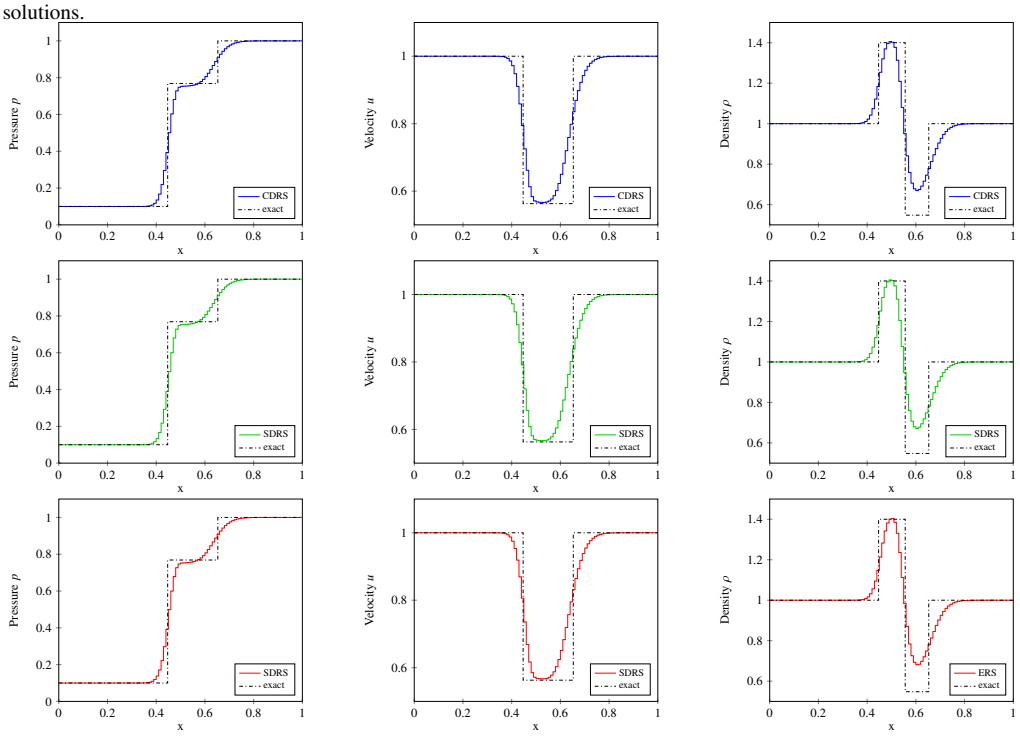

varying the artificial compressibility parameter c in the interval $[1, 1000]$. It is interesting to remark that SDRS shows significant errors when c is close to unit while errors tends to disappear while increasing c. This is expected since for a large c the velocity field is asymptotically solenoidal and, hence, the continuity equation is asymptotically equivalent to a transport equation for density (see Table 1). For the same reason the CDRS fluxes f_1 and f_3 tend to coincide with whose of ERS for $c \gg 1$. Instead, the momentum equation flux f_2 computed with CDRS shows a very large difference with respect to the ERS independently on the artificial compressibility value. This behaviour is to ascribe to the ρ_0 employed in the momentum equation.

Next we compare the solutions of a dG $\mathbb{P}^0$ discretization of the 1D artificial compressibility Euler equations which employs the proposed Riemann solvers at inter-element boundaries. In Figures 3, 4, 5, and 6 we compare dG $\mathbb{P}^0$ solutions with the exact solutions for test cases T1, T2, T3-T4, and T5, respectively, over a 100 elements grid of the unit line, *i.e.* $\Omega = [0, 1]$, with initial

Figure 4: DG $\mathbb{P}^0$ method with different Riemann solvers applied to test T2. Comparison between numerical and exact solutions.

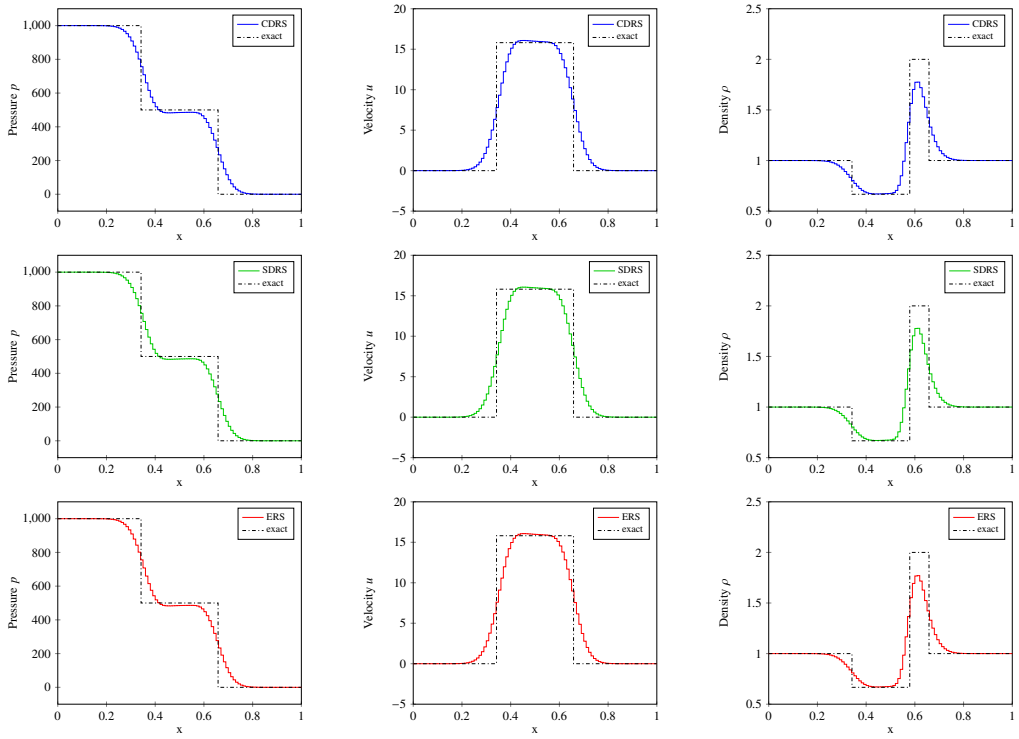

Figure 5: DG $\mathbb{P}^0$ method with different Riemann solvers applied to T3 (left) and T4 (right). Comparison between numerical and exact solutions.

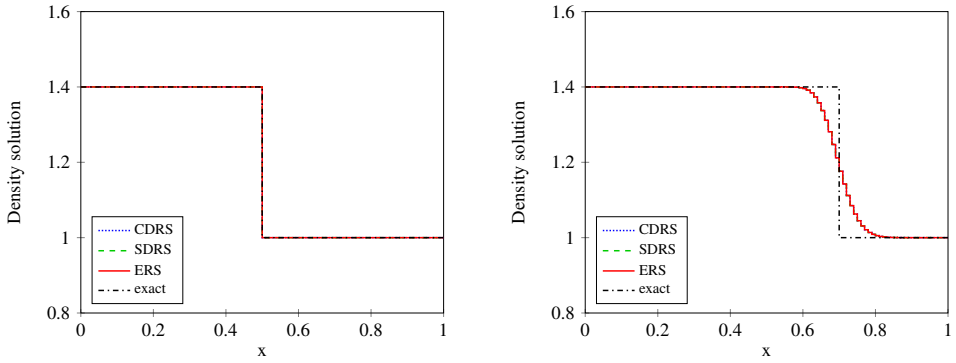

discontinuity at $x_0 = 0.5$.

As expected, the solutions provided for test cases T3 and T4 are equivalent for all the Riemann solvers and, in particular, for T3 the computed and the exact solutions coincide. Small, hardly

Figure 6: DG $\mathbb{P}^0$ method with different Riemann solvers applied to test T5. Comparison between numerical and exact solutions.

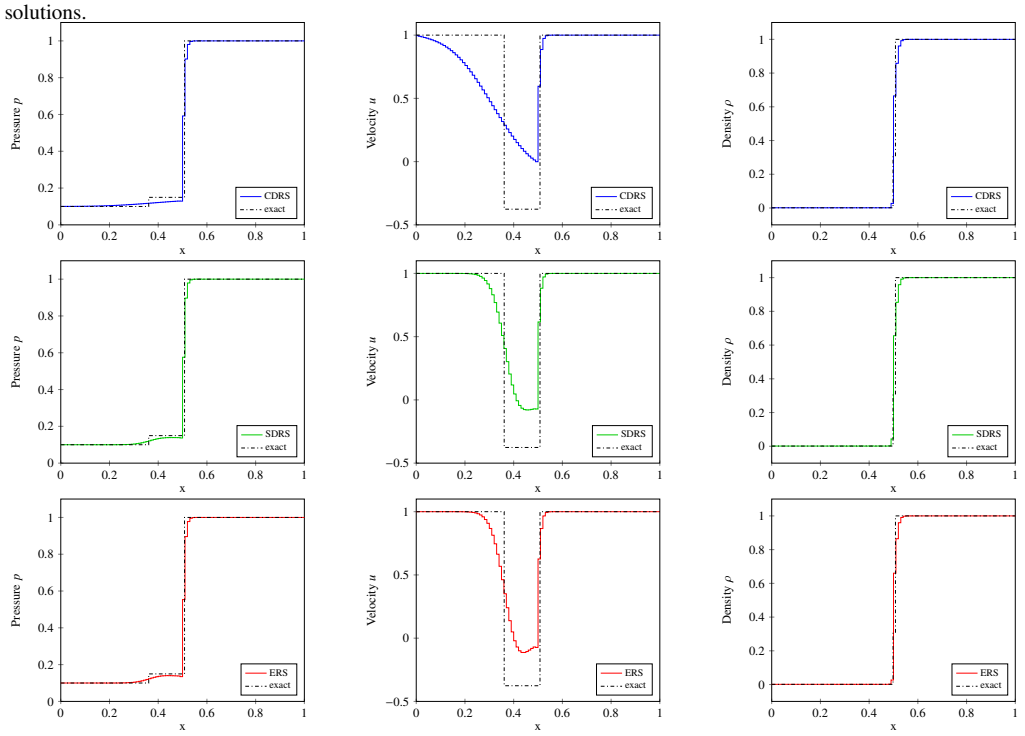

appreciable, differences are observed for T1 and T2, while it is evident that the most accurate numerical solution for T5 is obtained relying on the ERS.

In Figure 7 we evaluate convergence to the exact solution in "picture norm" considering a sequence of grids with $\{10^{i+1}\}, i = 1, 2, 3$ mesh elements. The exact solution is satisfactorily replicated on the finest grid here considered for test cases T1, T2 and T5. We do not consider test cases T3 and T4 because the exact solution is accurately reproduced on the coarsest grid (see Figure 5).

7.2. Kovasznay test case

In order to numerically validate the dG solver employing the exact Riemann solver at inter-element boundaries in two space dimensions we consider the Kovasznay test case [11] at Reynolds number 40 over $\Omega = [-0.5, 1.5]\times[0, 2]$. We consider the variable density incompress-

Figure 7: DG $\mathbb{P}^0$ method with the ERS applied to test T1, T2 and T5. Comparison between numerical and exact solutions on three grids of 100 ($grid_a$), 1000 ($grid_b$) and 10000 ($grid_c$) elements, respectively.

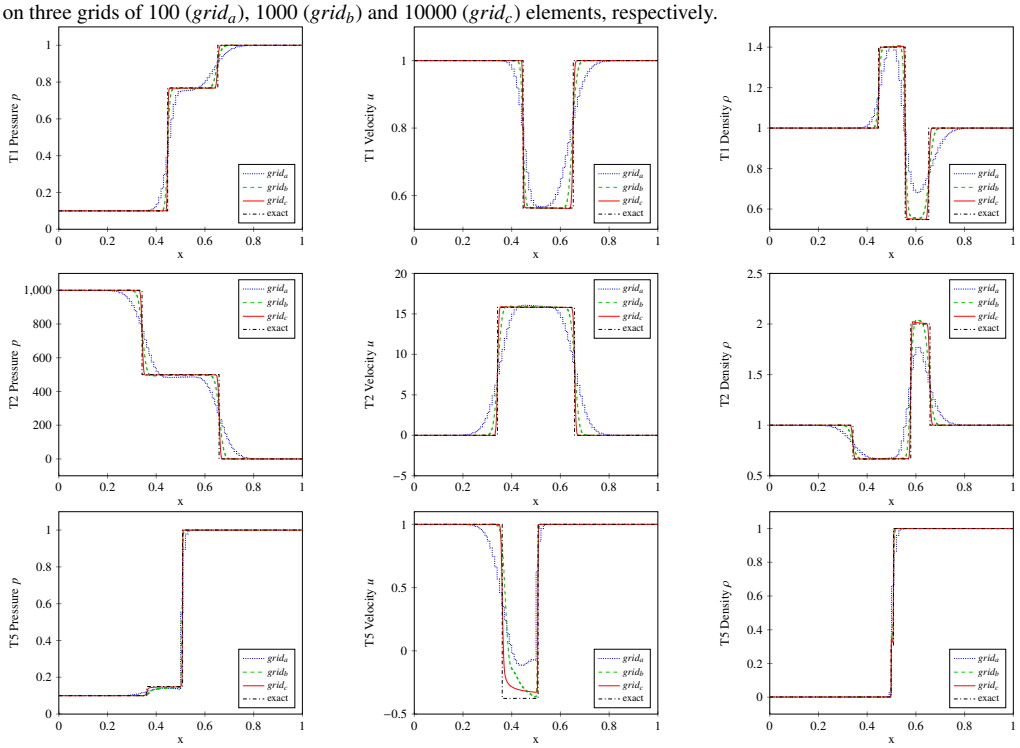

ible flow equations in Einstein notation

$$\begin{aligned} \frac{\partial u_j}{\partial x_j} &= 0, \\ \frac{\partial}{\partial t}(\rho u_i) + \frac{\partial}{\partial x_j}(\rho u_i u_j) &= -\frac{\partial p}{\partial x_i} + \frac{\partial \tau_{ij}}{\partial x_j} + \rho g_i, \\ \frac{\partial \rho}{\partial t} + \frac{\partial}{\partial x_j}(\rho u_j) &= 0, \end{aligned} \tag{105}$$

where $\mathbf{u} \in \mathbb{R}^d$ is the vector velocity, p is the pressure, ρ is the density and the viscous stress tensor reads

$$\tau_{ij} = 2\mu \left[\frac{1}{2} \left(\frac{\partial u_i}{\partial x_j} + \frac{\partial u_j}{\partial x_i} \right) - \frac{1}{3} \frac{\partial u_k}{\partial x_k} \delta_{ij} \right]. \tag{106}$$

The dG discretization for (105) can be obtained with the usual dG machinery, *i.e.*, multiply by a suitable test function, integrate by parts and introduce suitable numerical fluxes. For inviscid

Table 6: Kovasznay test case - Pressure (p), velocity components (u, v) and density (ρ) errors computed in L^2-norm with respective order of convergence for dG $\mathbb{P}^1$, $\mathbb{P}^2$, $\mathbb{P}^3$ and $\mathbb{P}^4$ space discretization on grids of 2^{2i} elements.

	i	err_p	order	err_u	order	err_v	order	err_ρ	order
$\mathbb{P}^1$	3	2.01E−3	–	7.91E−3	–	1.54E−3	–	2.11E−3	–
	4	5.88E−4	0.89	1.90E−3	2.06	4.29E−4	1.84	5.49E−4	1.94
	5	1.58E−4	1.90	4.38E−4	2.12	1.07E−4	2.00	1.21E−4	2.18
	6	4.10E−5	1.95	1.02E−4	2.10	2.54E−5	2.07	2.55E−5	2.25
	7	1.05E−5	1.96	2.43E−5	2.07	5.99E−6	2.09	5.51E−6	2.21
	8	2.69E−6	1.96	5.90E−6	2.04	1.43E−6	2.06	1.25E−6	2.14
$\mathbb{P}^2$	3	2.41E−4	–	4.22E−4	–	1.11E−4	–	1.16E−4	–
	4	6.46E−5	0.95	5.17E−5	3.03	1.56E−5	2.83	1.76E−5	2.72
	5	1.70E−5	1.93	6.53E−6	2.99	2.15E−6	2.86	2.36E−6	2.90
	6	4.41E−6	1.95	8.29E−7	2.98	2.87E−7	2.90	3.09E−7	2.94
	7	1.13E−6	1.97	1.05E−7	2.98	3.74E−8	2.94	3.98E−8	2.96
	8	2.86E−7	1.98	1.32E−8	2.99	4.78E−9	2.97	5.08E−9	2.97
$\mathbb{P}^3$	3	1.46E−5	–	3.45E−5	–	7.77E−6	–	2.11E−5	–
	4	1.47E−6	1.66	2.33E−6	3.89	5.34E−7	3.86	5.49E−7	3.69
	5	1.56E−7	3.24	1.50E−7	3.96	3.61E−8	3.89	1.21E−8	3.72
	6	1.79E−8	3.12	9.45E−9	3.98	2.41E−9	3.90	2.55E−9	3.91
	7	2.16E−9	3.05	5.93E−10	3.99	1.58E−10	3.93	5.51E−10	4.06
	8	2.67E−10	3.02	3.72E−11	4.00	1.02E−11	3.95	1.25E−10	4.17
$\mathbb{P}^4$	3	1.50E−6	–	1.05E−6	–	2.82E−7	–	6.36E−7	–
	4	1.13E−7	1.86	3.22E−8	5.03	9.57E−9	4.88	2.51E−8	4.66
	5	7.83E−9	3.86	9.93E−10	5.02	3.04E−10	4.97	9.11E−10	4.79
	6	5.13E−10	3.93	3.09E−11	5.01	9.47E−12	5.01	2.99E−11	4.93
	7	3.28E−11	3.97	9.66E−13	5.00	2.94E−13	5.01	9.12E−13	5.04
	8	2.08E−12	3.98	3.02E−14	5.00	9.13E−15	5.01	2.63E−14	5.12

fluxes we consider the Godunov fluxes obtained by means of the Exact Riemann Solver ERS while for viscous fluxes we employ the BR2 method of [2].

We consider first, second, third, and fourth polynomial degree dG discretizations on a sequence of h-refined grids with 2^{2i}, $i = 3, 4, ..., 8$ quadrilateral elements and report the convergence rates in Table 6. The expected convergence rates of h^k for the pressure error in L^2 norm and h^{k+1} for the velocity and the density error in L^2 norm are confirmed by numerical results. All the results reported in Table 6 have been obtained setting $c = 1$ and we verified that the same convergence rates are observed choosing $c = 10^{\pm\frac{j}{2}}$ with $j = 0, 1, ..., 6$. The influence of c on the pressure, velocity and density errors are reported in Figure 8 considering a 32x32 quadrilateral elements grid. While velocity errors are almost independent from the choice of c, pressure and density

Figure 8: Kovasznay test case. Numerical errors on pressure (p), velocity components (u, v) and density (ρ) solutions computed for different artificial compressibility c values on grid 32x32 with dG $\mathbb{P}^1$, $\mathbb{P}^2$, $\mathbb{P}^3$, $\mathbb{P}^4$ space discretization.

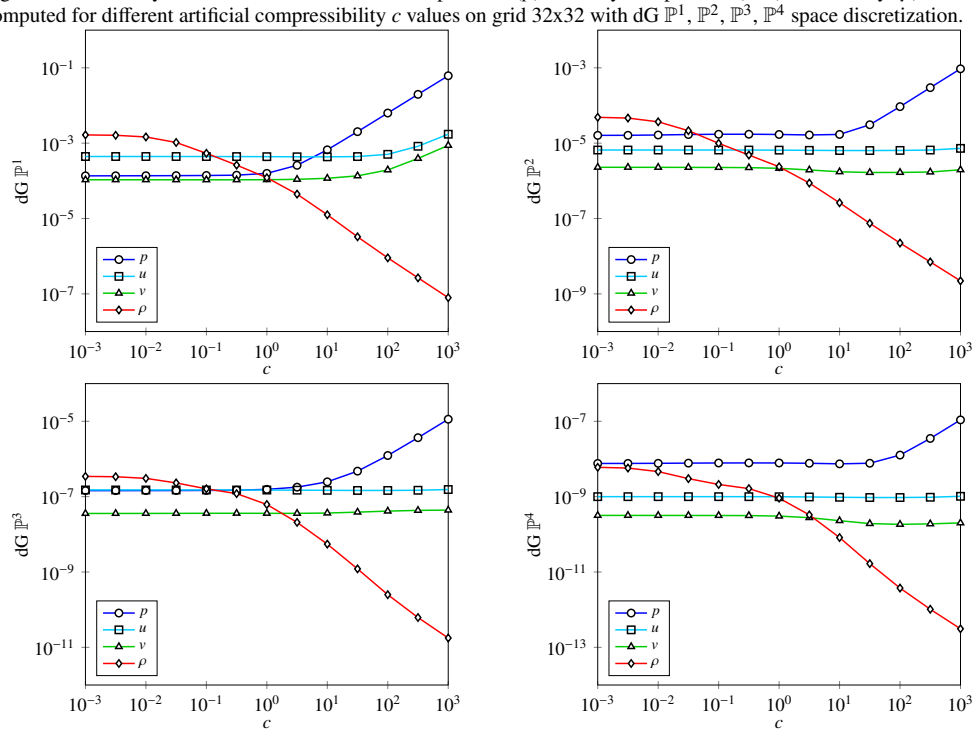

errors behave in an opposite fashion. The density error decreases linearly for $c > 1$ while the pressure error increases linearly for $c >> 1$. Note that the pressure error increase shifts towards higher values of c while increasing the polynomial degree. Overall the numerical results confirm that it is safe to choose c close to unit if smooth solutions are expected.

7.3. The Rayleigh–Taylor instability test case

In this section we assess the performance of the proposed dG method on the variable density flow problem of the Rayleigh–Taylor instability (RTI). This test case consists of two layers of immiscible fluids initially at rest and evolving under the effect of the downward gravity field. The density ratio is set to 3, hence the Atwood number, defined as $At = (\rho_{max} - \rho_{min})/(\rho_{max} + \rho_{min})$, is equal to 0.5 [15]. Following Guermond and Quartapelle [9], the transition between the two

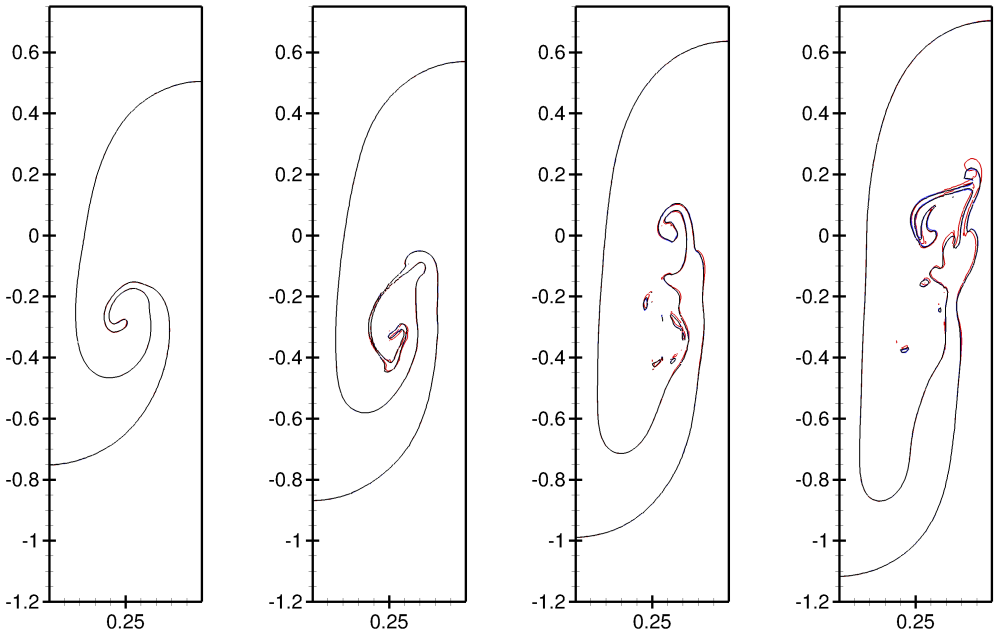

(a) $t = 1.75$ (b) $t = 2$ (c) $t = 2.25$ (d) $t = 2.5$

Figure 9: RTI test case. Influence of the c value on the $\rho = 2$ isoline for the $Re = 1\,000$ $\mathbb{P}^4$ solution. Red line: $c = 1$, blue line: $c = 10$, black line: $c = 1000$.

fluids is regularized according to the law

$$\frac{\rho(x, y, t = 0)}{\rho_0^{min}} = 2 + \tanh\left(\frac{y - \eta(x)}{0.01d}\right), \tag{107}$$

where $\eta(x) = -0.1d\cos(2\pi x/d)$ is the initial position of the perturbed interface between the two fluids, and d is a reference length ($d = 1$ in our computational domain). The L^2 projection of this analytical density distribution on the solution polynomial space provides the initial density field. The solutions have been computed on a Cartesian mesh with 16×128 quadrilateral elements, imposing symmetry conditions on all the boundaries of the rectangular domain $\Omega = [0, 0.5]\times[-2, 2]$. All the simulations have been integrated in time with a high-order linearly-implicit, fourth-order, six-stage Rosenbrock scheme [1] with 447 time steps per time unit of Tryggvason [15].

The time history of the density contours at times $t = \{1, 1.5, 1.75, 2, 2.25, 2.5\}$ in the scale of

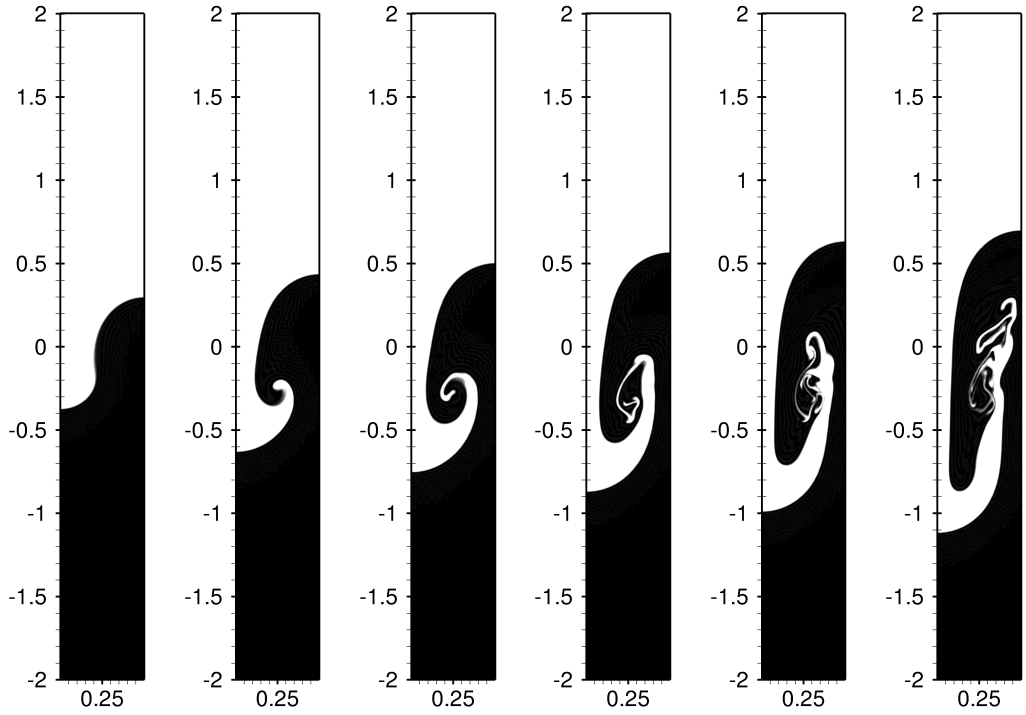

(a) $t = 1$ (b) $t = 1.5$ (c) $t = 1.75$ (d) $t = 2$ (e) $t = 2.25$ (f) $t = 2.5$

Figure 10: RTI test case. $Re = 1\,000$, time history of the density contours, $c = 10$, $\mathbb{P}^6$ solution.

Tryggvason are shown in Figs. 10 and 11 for the $Re = 1\,000$ and $Re = 5\,000$ cases, respectively. These results were obtained with $c = 10$ and a $\mathbb{P}^6$ polynomial approximation resulting in 57 344 degrees of freedom. This value of c was chosen on the basis of preliminary results for the case $Re = 1\,000$ with $\mathbb{P}^4$ polynomial approximation. For this case we assessed the influence of the artificial compressibility parameter by comparing the time evolution of the density isoline $\rho = 2$ for the set of values $c = \{1, 10, 1000\}$ reported in Figure 9. A close look at this time history reveals that the solutions for $c = 10$ and $c = 1000$ appear almost superimposed, while for $c = 1$ the solution is slightly different with the lighter fluid penetrating more in depth into the plume. Since the c sensitivity study performed on the Kovasznay test case showed that low c values are preferable, and since high values of c deteriorate the convergence of the linear solver, we decided to set $c = 10$ in all the following viscous computations.

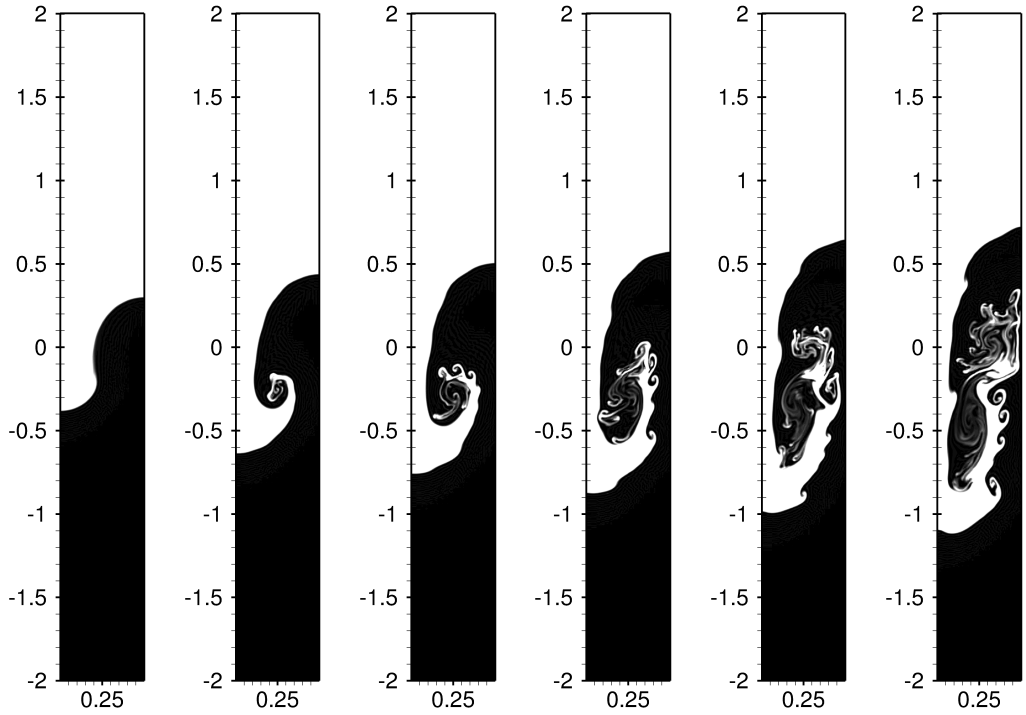

(a) $t = 1$ (b) $t = 1.5$ (c) $t = 1.75$ (d) $t = 2$ (e) $t = 2.25$ (f) $t = 2.5$

Figure 11: RTI test case. $Re = 5\,000$, time history of the density contours, $c = 10$, $\mathbb{P}^6$ solution.

The solutions for $Re = 1\,000$ are in reasonable agreement with the results of Guermond and Salgado [10] obtained with much more degrees of freedom on a mesh of 235 552 triangles with a third-order finite elements approximation resulting in 466 572 nodes. Although the height reached by the plume of the high-density fluid for the $Re = 5\,000$ case is similar to their results, our computations show more wiggles at the interface between the two fluids. The results of the inviscid version of this test were slightly more dependent on the artificial compressibility parameter value as shown in Fig. 12 for the time levels $t = 1.75$ and $t = 2.25$. We remark that all the computations presented in this work have been performed without any stabilization technique to control possible spurious oscillations around sharp density gradients. The implementation of suitable techniques for the control of spurious oscillations will be the subject of future work.

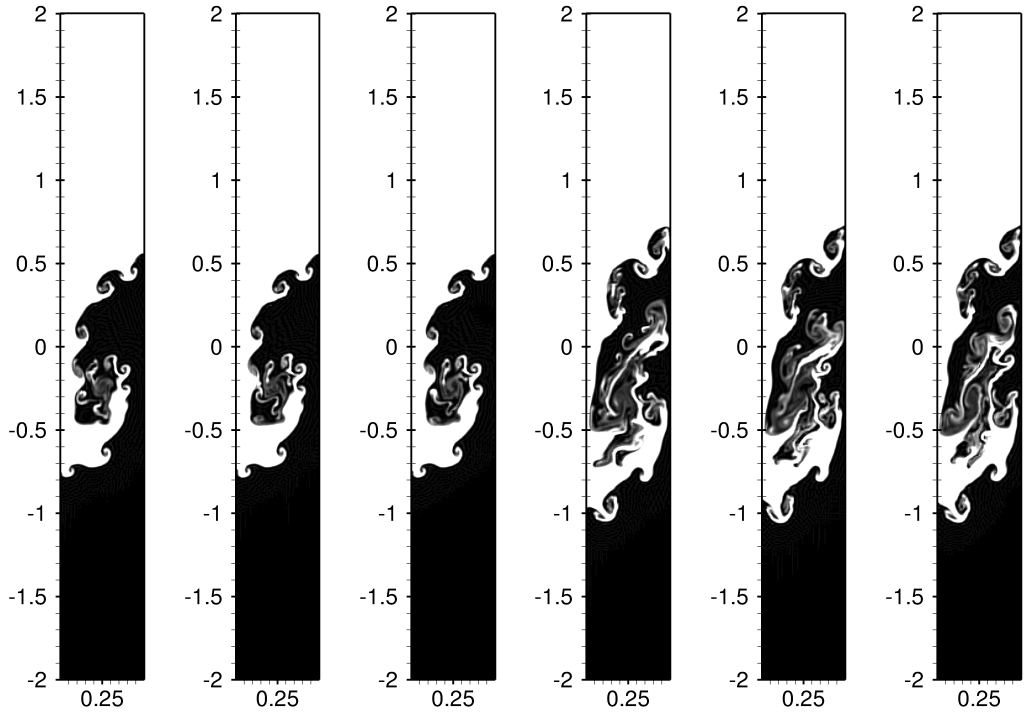

(a) $c = 1$ (b) $c = 10$ (c) $c = 1000$ (d) $c = 1$ (e) $c = 10$ (f) $c = 1000$

Figure 12: RTI test case. Influence of the c value on the density contours for the inviscid case at time levels $t = 1.75$ (Figs. 12(a)–12(c)) and $t = 2.25$ (Figs. 12(d)–12(f)) , $\mathbb{P}^4$ solution.

8. Conclusions

In this work we presented three Riemann solvers for the artificial compressibility perturbation of the 1D variable density incompressible Euler equations and we extended the dG discretization of the INS equations proposed by Bassi et al. [3] to cope with variable density incompressible flows. Among the proposed solvers, the exact Riemann solver is of particular interest, both from the accuracy and the efficiency viewpoint. It admits an explicit exact solution, therefore it does not require iterative solutions of nonlinear equations. As a welcome side effect, the ability to manufacture exact solutions can be exploited for validation purposes.

The Riemann solvers here devised can be employed in the context of numerical formulations relying on Godunov fluxes which are solution of local Riemann problems arising at inter-element boundaries. Using the exact Riemann solver to compute the inviscid fluxes for the velocity-

pressure-density triad in the framework of a high-order accurate dG discretization of the variable density INS equations, the convergence properties of the method have been demonstrated by extensive computations of the Kovasznay test case. The influence of the artificial compressibility parameter on the error with respect to the exact solution has been investigated. Challenging numerical solutions of the Rayleigh-Taylor instability problem have been obtained at different Reynolds numbers showing good agreement with previously published results. The inviscid flow regime was also addressed to demonstrate the robustness of the dG formulation here proposed.

Since the inviscid Godunov numerical fluxes provided by the exact Riemann solver are explicitly available, also the relation between the star region solution and the left and the right states can be explicitly determined. Accordingly, the numerical fluxes are well suited to be employed in the context of hybrid and hybridizable dG formulations relying on inter-element unknowns. This extension will be the subject of future work.

[1] F. Bassi, L. Botti, A. Colombo, A. Ghidoni, F. Massa, Linearly implicit Rosenbrock-type Runge–Kutta schemes applied to the Discontinuous Galerkin solution of compressible and incompressible unsteady flows. Comput. Fluids, 118:305–320, 2015.

[2] F. Bassi, S. Rebay, G. Mariotti, S. Pedinotti, M. Savini, A high-order accurate discontinuous finite element method for inviscid and viscous turbomachinery flows, in: R. Decuypere, G. Dibelius (Eds.), Proceedings of the 2nd European Conference on Turbomachinery Fluid Dynamics and Thermodynamics, Technologisch Instituut, Antwerpen, Belgium, (1997) 99–108.

[3] F. Bassi, A. Crivellini, D. A. Di Pietro, S. Rebay, An artificial compressibility flux for the discontinuous Galerkin solution of the incompressible Navier-Stokes equations, J. Comput. Phys. 218 (2006) 794–815.

[4] F. Bassi, A. Crivellini, D. A. Di Pietro, S. Rebay, An implicit high-order discontinuous Galerkin method for steady and unsteady incompressible flows, Comput. Fluids 36 (10) (2007) 1529–1546. doi:http://dx.doi.org/10.1016/j.compfluid.2007.03.012.
URL http://www.sciencedirect.com/science/article/pii/S0045793007000400

[5] L. Botti, A. Colombo, F. Bassi, h-multigrid agglomeration based solution strategies for discontinuous Galerkin discretizations of incompressible flow problems, submitted for publication, arXiv:1703.03592 (2017).

[6] A.J. Chorin, A numerical method for solving incompressible viscous flow problems, J. Comput. Phys. 2 (1) (1967) 12–26.

[7] A. J. Chorin, Numerical solution of the Navier–Stokes equations, Math. Comp. 22 (1968) 745–762.

[8] D.T. Elsworth, E.F. Toro, Riemann solvers for solving the incompressible Navier-Stokes equations using the artificial compressibility method, College of Aeronautics, Cranfield Institute of Technology, 9208 (1992).

[9] J.-L. Guermond, L. Quartapelle, A projection FEM for variable density incompressible flows, J. Comput. Phys. 165 (1) (2000) 167–188.

[10] J.-L. Guermond, A. Salgado, A splitting method for incompressible flows with variable density based on a pressure Poisson equation, J. Comput. Phys. 228 (8) (2009) 2834–2846.

[11] L.S.G. Kovasznay, Laminar flow behind a two-dimensional grid, Proc. Camb. Philos. Soc. 44 (1948) 58–62.

[12] Jae-Hong Pyo, Jie Shen, Gauge-Uzawa methods for incompressible flows with variable density, J. Comput. Phys. 221 (1) (2007) 181–197.

[13] R. Temam, Sur l'approximation de la solution des équations de Navier–Stokes par la méthode des pas fractionnaires, Arch. Ration. Mesh. Anal. 33 (1969) 377–385.

[14] E.F. Toro, Riemann solvers and numerical methods for fluid dynamics: a practical introduction, Springer Science & Business Media, 2013.

[15] G. Tryggvason, Numerical simulations of the Rayleigh-Taylor instability, J. Comput. Phys. 75 (2) (1988) 253–282. doi:http://dx.doi.org/10.1016/0021-9991(88)90112-X.
URL http://www.sciencedirect.com/science/article/pii/002199918890112X